Transpiration-Cooling with Porous Ceramic Composites in Hypersonic Flow

Hannah Böhrk
Institute of Structures and Design
German Aerospace Center (DLR)
Pfaffenwaldring 38-40
70569 Stuttgart
Germany

hannah.boehrk@dlr.de

Contents

INTRODUCTION

Space flight requires high performance materials with high strength to density ratio over a wide temperature range. The definition of the high temperature, however, depends on the application. In terms of satellite systems, for example, high temperature can be anything above 450 K, while this is perceived as a low temperature in rocket engine technology or structural response at hypersonic flight. Ground based high temperature applications, include fire fighting, where the thermal emergency conditions exceed 600 K, power plants and incinerators operating at up to 1100 K, and modern gas turbines are run at temperatures up to 2500 K for increased efficiency and reduced emission. Extreme environment is also faced during high-speed flight or in engines and rockets. The wall temperatures currently endured are roughly 3500 K in the hot combustion zone and a few hundred Kelvin in the cooled exterior of the chamber wall and approximately 2000 K on short-term exposed vehicle leading edges.

Deutsches Zentrum für Luft- und Raumfahrt (DLR, German Aerospace Center) has been investigating ceramic rocket motors since the 1990s [1, 2]. The experience with this technology has led to the transpiration-cooling of other hot structures, such as thermal protection systems (TPS) for atmospheric re-entry manoeuvres. The fiber ceramic C/C-SiC used for the SHEFEX II TPS is manufactured in house at DLR-BK. It is a composite consisting of carbon fibers with a matrix of carbon and silicon carbide. It has been qualified in plasma wind

tunnel testing and during real re-entry flight, such as in the FOTON 9, EXPRESS, FOTON-M2, and SHEFEX missions. Moreover, with AKTiV, the first transpiration cooling flight experiment was flown on SHEFEX II in a sub-orbital re-entry mission in 2012 [3].

The present manuscript is based on and profits from this broad experience. It is an extended version of the book chapter [4]. Fruitful help was provided by my colleagues Henning Elsäßer, Sofia Giagkozoglou, Christian Dittert, Daniel Prokein, Simon Vandevelde, and Dr.-Ing. Stefan Löhle.

Chapter 1 gives an overview over the loads on hypersonic vehicles, putting into relation the two typical hypersonic flight situations atmospheric re-entry flight and hypersonic cruise flight. In chapter 2, an approach of determining the thermal structural response of hot structures for their proper layout is introduced. This approach is realized in the program HEATS which serves later to interpret flight data. Chapter 3 gives a brief overview over reinforced ceramic matrix composites often used as structural material for hypersonic applications. Chapter 4 gives flight data from AKTiV on SHEFEX II. The data and evaluation show that AKTiV has successfully demonstrated transpiration-cooling during atmospheric re-entry and proven high efficiency. Transferring the findings from one-dimensional ground-based and flight experiments to the multidimensional critical components of hypersonic vehicles, such as leading edges, additional considerations have to be made. Chapter 5 discusses the coolant mass flow distribution in orthotropic material in three-dimensional structures when pressure and thermal gradients occur.

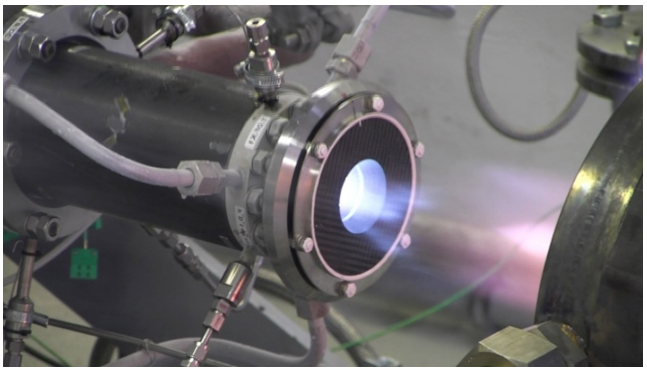

DLR's transpiration-cooled composite thrust chamber during a 20 s representative demonstration test at the P6.1 test facility (MT5-A campaign) in 2011. Chamber pressure p_c = 55 bar, oxide-to-fuel-ratio = 5.5 with liquid oxygen and gaseous hydrogen (9% fed through the permeable combustion chamber lining) [2]

Transpiration-cooled experiment AKTiV on SHEFEX II.

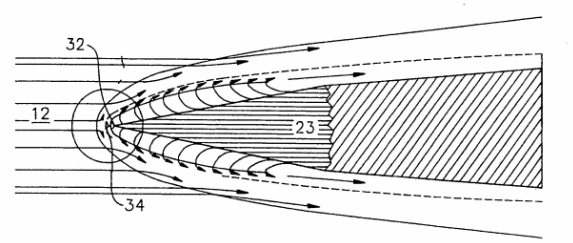

Transpiration-cooled Leading Edge as sketched by Bulman.

The development of high temperature management is ongoing and the examples shown here make no claim to be complete. New and improving solutions are always possible. Have you got an idea?

1 HYPERSONIC FLIGHT

Hypersonic velocities are encountered during atmospheric re-entry flight or during sustained hypersonic flight. Both are connected with flight in the atmosphere, where the large velocities of the vehicle causes a shock or a bow shock wave ahead of the vehicle. Through this shock, the atmospheric gas is compressed and the kinetic energy is dissipated into internal energy of the atmospheric gas.

Hypersonic velocity is generally defined as velocities of Mach 5 or greater and implies effects such as narrow shocks, with shock distances so small that the shock layer may interact with the boundary layer, or high temperature effects in which the atmospheric gas is decomposed by dissociation of the molecules and ioniziation of flow particles. It was found in the 1950s by H.J. Allen that the shock distance δ to the vehicle surface increases with the nose radius which drastically decreases heat load. Oertel gives the correlation [5]

$$\delta = R_{LE} 0.143 e^{3.24/M^2} \tag{1}$$

for hypersonic flight with Mach number M and the leading edge radius R_{LE}.

A few vehicles having performed successful re-entry are shown in figure 4. Typical entry velocities v range from 7.9 km/s for an Earth orbital re-entry and over 11.3 km/s for a return mission from another celestial body. The kinetic enthalpy

$$h = \frac{1}{2} v^2 \tag{2}$$

amounts to approximately 31 MJ/kg, and 63 MJ/kg, respectively.

Re-entry vehicles are, in principle, deceleration systems, the most prominent one being the Space Shuttle [6]. The challenge of the atmospheric re-entry is decreasing the vehicle's velocity from 7.9 km/s (28,000 km/hr) in flight to 0 km/s on ground only by deceleration in terms of drag and friction. This can be achieved by a ballistic re-entry trajectory, in which the vehicle falls at high velocity back into the atmosphere and thus encounters strong deceleration loads and a high heat flux onto the vehicle's protective material over a short period of time. Deceleration can also be achieved by a lifted re-entry, in which the strategy is to decrease velocity at higher altitude, where the atmosperic density is still relatively low, and thus encounter only a reduced amount of heat flux. In figure 5, both re-entry strategies are sketched. Therefore, the most vehicles are blunt in design in order to achieve large drag and a large shock stand-off distance ahead of the vehicle. In the distance between the shock layer and the vehicle surface, the energy is dissipated into internal degrees of freedom of the atmospheric gas, i.e. dissociation, vibration and rotation, causing a reduction of the sensible temperature of the gas for the vehicle surface.

Figure 4: *Re-entry vehicles: a) Apollo, b) Stardust, which performed hyperbolic re-entry in 2006 after having collected dust from the coma of comet Wild 2, c) European re-entry vehicle ARD (Atmospheric Re-entry Demonstrator), which completed re-entry flight from a sub-orbital mission after launch with Ariane 5, d) Space Shuttle, which operated on 135 missions from 1981 to 2011.*

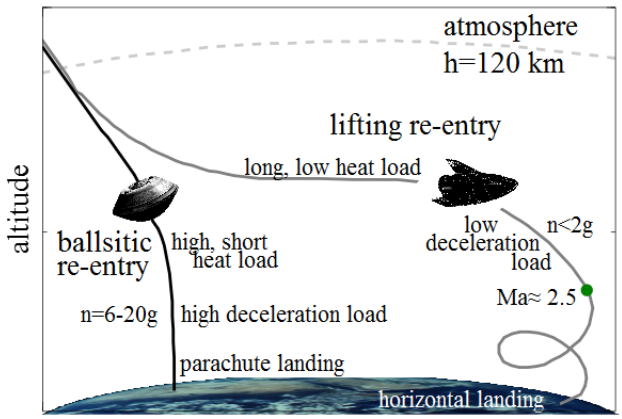

Figure 5: *Ballistic and lifted re-entry strategies.*

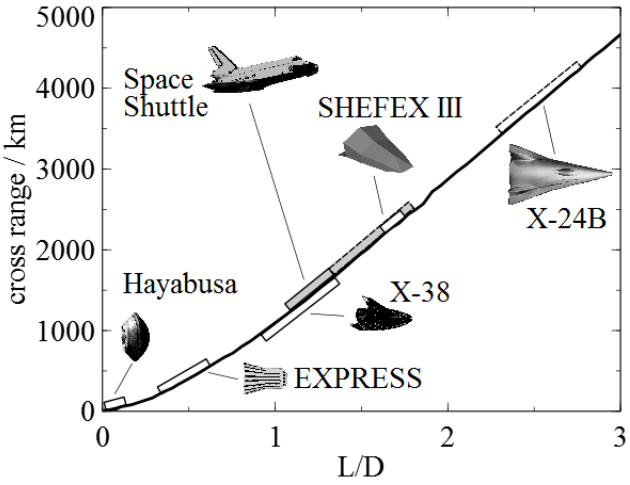

Figure 6: *Cross range capabilities for hypersonic lift-to-drag ratio for hypersonic flight vehicles.*

Capsule-type re-entry vehicles typically have axissymmetric shape and fly at negative angle of attack, resulting in weak aerodynamic performance, the measure of which is the lift-to drag ratio L/D. This parameter governs mission capabilities, such as down and cross range. Figure 6 shows cross range capabilities of hypersonic vehicles. Wingless re-entry vehicles generate aerodynamic lift from the shape of their bodies. With research missions of the X-24A in the 1960s, it was demonstrated that hypersonic vehicles like the Space Shuttle could land on conventional runways by only gliding. The X-24B was intended to test lifting body concepts at very high lift-to-drag ratio. Lifting re-entry bodies have flat lower sides and fly at large postitive angles of attack, resulting in an aerodynamic performance L/D between 0.5 and up to and above 2.0.

As opposed to re-entry vehicles, hypersonic cruise vehicles must, like aircraft, fly with efficient propellant consumption. The technology is currently evolving. Hypersonic cruise vehicles have to have minimum aerodynamic drag in order to be propellant efficient, which for hypersonic flight necessitates a slender configuration. In order to develop a high-Machnumber powered transportation system, scramjet technology (among others) is extended. Demonstrators of scramjet flight tests were HyShot II and III, flown in 2002 and 2006 at Mach 7.6, the two NASA X-43 vehicles, both flown in 2004 at Mach 7 and 10, and X-51 flown at Mach 5.1 in 2013. In the ongoing effort to achieve faster air-breathing propulsion systems, combustion and considerable thrust at higher Mach numbers (M∼8-12) has to be achieved [7]. The challenges are ignition and sustained combustion of fuel in scramjet engines at these flight speeds and high-altitude conditions (∼30km) with thinner atmosphere. Equation (1) shows that a shock stands ahead of blunt shapes but may be attached to pointed shapes, showing that leading edges of hypersonic cruise vehicles see very high heat load.

A formulation developed by Marvin and Pope is widely used for determining heat flux [8]

$$\dot{q} = K\sqrt{\frac{p_{tot}}{R_{\text{eff}}}}h \tag{3}$$

for the stagnation region of a hypersonic vehicle with flight enthalpy h, efficient leading edge radius R_{eff}, total pressure p_{tot} and a gas specific constant K, which is $0.368\,\text{kW kg}\,(\text{MJ m})^{-1}(\text{m Pa})^{-1/2}$ in the case of air. The heat flux to the leading edge is depending on the leading edge radius proportional to a root function, as depicted in figure 7.

Figure 8: *Payload of the SHEFEX II re-entry vehicle on the launcher on June 22nd 2012.*

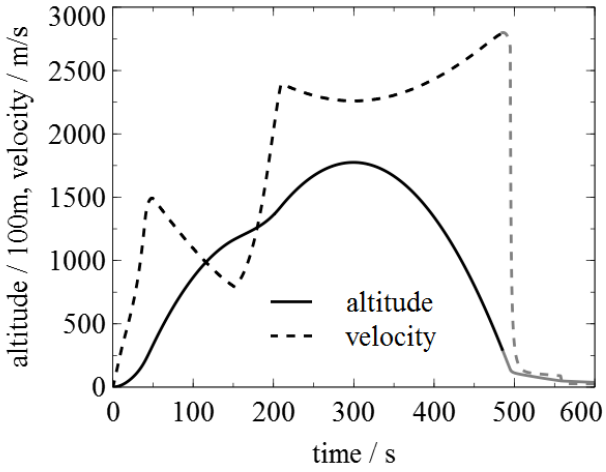

Figure 9: *DMARS data of the SHEFEX II trajectory. Black lines give in-flight measurement, gray lines give the assumed subsequent flight path [16].*

From an aerothermodynamic point of view, sharp leading edges of the slender, long vehicles can cause problems. They promote local stagnation areas with very high temperatures which materials previously have not withstood. During the 1990s, the development of ceramic composites and ultra high temperature materials for TPS applications led to a renewed interest in sharp edged configurations [9] such as the waverider concept DLR F8 [10], the DLR-ONERA project JAPHAR [11] or the lifting body concept HL-20 and the SHARP project, both from NASA [12, 13]. Adding to these issues is the slender aerodynamic shape of minimum drag which provides thin cross-sections at elevated temperatures. One of the primary thermomechanical challenges results from large thermal gradients, for example at attachments of hot structures to an airframe, as was described in the former chapter.

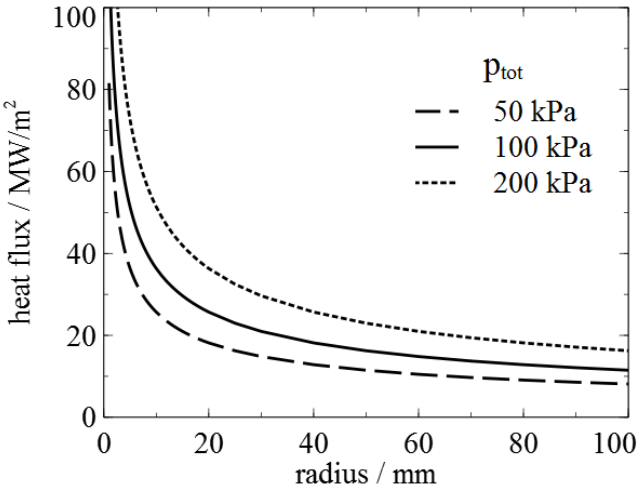

Figure 7: *Heat flux dependency on leading edge radius for orbital re-entry.*

The DLR program Sharp Edge Flight Experiment (SHEFEX) comprises a series of platforms for re-entry experiments. The faceted concept of SHEFEX intends to reduce the design and manufacturing cost of the ceramic matrix composite (CMC) thermal protection system [14, 15]. Figure 8 shows the geometry of SHEFEX II with a fore-body of ogive form and octagonal cross-section. The forebody is symmetrically divided into eight identical facets 1 through 8 in circular direction in all five segments A through E, as marked in Figure 10. It performed sub-orbital re-entry from a 177 km apogee. The total flight time was roughly 500 s comprising 52 s of experimental time for the atmospheric re-entry between 100 and 30 km. Within the experiment time, the vehicle accelerated from 2559 m/s and Mach 10.2 at 101 km altitude to 2791 m/s and Mach 9.3 at 30 km. The trajctory is shown in Figure 9.

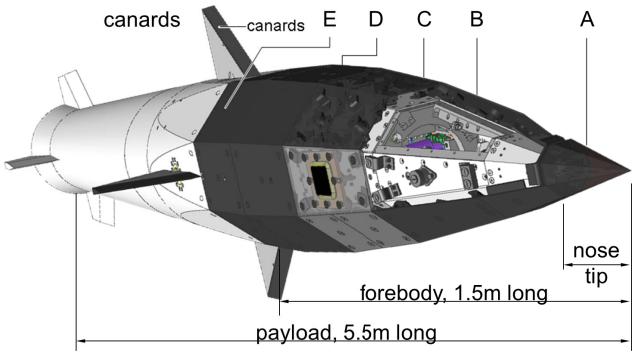

Figure 10: *SHEFEX II re-entry vehicle.*

The 1.5-m-long forebody of SHEFEX II has a sharply pointed nose tip made from solid C/C-SiC, the vehicle's leading edge. As discussed above, sharp leading edges are subject to severe aerodynamic heating since the shock attaches to the pointed structure. The challenge for the designer is thus the determination of the thermomechanical load onto the structure, the choice of the cooling method, material choice, attachment, and instrumentation. In case of SHEFEX II, it is sufficient for the nose and canard to be radiation cooled and a recession of up to a few millimeters is tolerated.

One key experiment of SHEFEX II was the transpiration-cooled experiment AKTiV. The experiment is also visible in Figure 10 with a black permeable sample, while in Figure 8 the sample appears lighter than the surrounding panel. The next section will introduce a heat balance approach to the structural thermal response while the material choice for AKTiV is explained in the subsequent section.

2 STRUCTURE THERMAL RESPONSE

In order to design a thermal protection system, the thermal response of the material to the load has to be known. Depending on the mission, transient wall temperature determination is essential in order to optimize thermal protection system (TPS) mass. However, for horizontal hypersonic cruise flight at likely invariant flight and atmospheric conditions, a steady state of the TPS is approached.

The heat equation in two dimensions, with density ρ, heat capacity c, temperature T and thermal conductivity λ in x and y direction

$$\rho\, c\, \frac{\partial T}{\partial t} = \lambda_y \frac{\partial^2 T}{\partial y^2} + \lambda_x \frac{\partial^2 T}{\partial x^2}\,, \tag{4}$$

can serve as an approach to describe the temperature development at any point within the TPS material. In the case of a steady-state problem, $\frac{\partial T}{\partial t}$=0. Boundary condition is the heat balance at the surface and a boundary condition of second order can, for example, be used at the rear side and the edges of the TPS-panels

$$\lambda_y \left(\frac{\partial T}{\partial y}\right)_{rear} = 0\,, \tag{5}$$

i.e. assuming that these sides are adiabatic.

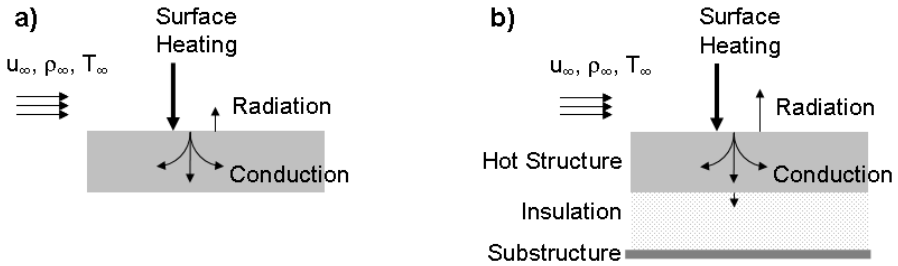

Figure 11: *a) Capacitive cooling and b) radiative cooling.*

Figure 11 a) illustrates a capacitively cooled thermal protection system that manages the heat by a thick wall of material that has high heat capacity. This is used for low heat fluxes and relatively short mission times. Radiation of the vehicle surface (index S) can be modelled by a gray body assumption,

$$\dot{q}_{rad} = \sigma \epsilon T^4 \tag{6}$$

with Stefan-Boltzmann-constant σ and the wall material's emissivity ϵ. However, for capacitive cooling, surface temperatures are usually low and thus, radiative heat flux on these structures is marginal. If a heat sink structure is heated for a long period of time, enough heat could be absorbed to overheat the structure. Figure 11 b) shows a radiatively cooled system which is used for example in the EXPERT (European Experimental Re-Entry Testbed) nose cap or the SHEFEX TPS. A view of the SHEFEX TPS is given in figure 12 [17].

Thermal radiation, as a mechanism to remove the heat, becomes more efficient with higher temperature. The emissivity has strong influence on the surface radiation cooling. In contrast to a heat sink structure, hot structures with significant radiation cooling can be used for a higher heat load, allowing the structure to reach steady state conditions. Again, the heat is both radiated away and conducted inward. The objective of the insulation is to minimize the amount of heat reaching the structure. Figure 11 indicates that a small amount of heat is conducted through the insulation to the structure. Boundary condition (5) now applies at the rear of the insulation.

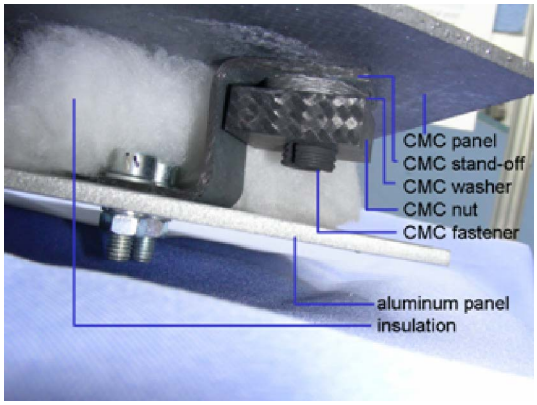

Figure 12: *SHEFEX II thermal protection system set-up [17].*

The heat balance for the surface in the case of the capacitively and radiatively cooled systems assumes that all incoming heat flux $\dot{q}_{HG-S}$ from the hot gas (HG) to the surface (S) is either conducted into the structure, $\dot{q}_{cond}$, or radiated away, $\dot{q}_{rad}$, so that [18]

$$\dot{q}_{HG-S} = \dot{q}_{rad} + \dot{q}_{cond}\,. \tag{7}$$

Heat flux from the flow to the wall can be convective heat flux, radiation, or chemical effects such as catalysis. In the present approach these effects are neglected and only convective heat flux is looked at. The thermal energy input rate

$$\dot{q}_{HG-S} = \alpha_A\,(T_r - T_S) \tag{8}$$

is transferred from the hot gas to the wall through convection with the heat transfer coefficient α_A and the recovery temperature T_r. These parameters are functions of the flow properties and can be expressed by means of the ambient velocity u_∞, gas density ρ_∞, specific heat $c_{p,\infty}$, and the Stanton number St as

$$\alpha_A = St\rho_\infty c_{p,\infty} u_\infty \tag{9}$$

and

$$T_r = T_\infty\left(1 + r\frac{\kappa-1}{2}M_\infty^2\right)\,, \tag{10}$$

with the isentropic coefficient κ. The two commonly unknown variables of Eqs. (9) and (10) are the Stanton number St and the recovery factor r. They must be determined for each flow condition, be it laminar or turbulent. This can done based on known models of Crocco and van Driest [18–20] The boundary condition at the surface S is

$$\dot{q}_{cond} = \lambda_y\left(\frac{\partial T}{\partial y}\right)_S\,. \tag{11}$$

If hot structure has to withstand extreme heat load for long times, passive radiation or heat sink cooling is not sufficient anymore. The X-15, for example, used Inconel as a heat sink for thermal protection, and suffered skin penetration due to high temperatures generated from shock-shock interactions [21]. One possible solution to reduce temperatures at the surface is the backface cooling of the hot structure. This can even be realized in a semi-passive thermal protection system using a heat pipe. Heat is transferred by a working fluid to another region of the heat pipe where the heat is radiated away. Figure 13 shows the heat transfer mechanisms for the heat pipe. All processes remain the same as with radiative or capacitive cooling, but the boundary condition between hot material and working fluid is now

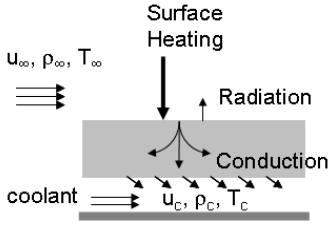

Figure 13: *Heat pipe cooling.*

$$\dot{q}_{cond} = \dot{q}_{rear-C} + \dot{q}_{rad}\,, \tag{12}$$

with index $rear - C$ indicating convective heat transfer from the wall to the coolant. Heat flux $\dot{q}_{rear-C}$ can, again, be estimated as $St\rho_c c_{p,c} u_c(T_{rear} - T_{r,c})$.

Active cooling is required for even higher heat fluxes and for longer mission times. Convective cooling of the hot surface, in which the coolant heats up and carries the heat away, is also utilized for a high heat flux and long times. The structure operates hot but is maintained within its structural limits with respect to temperature

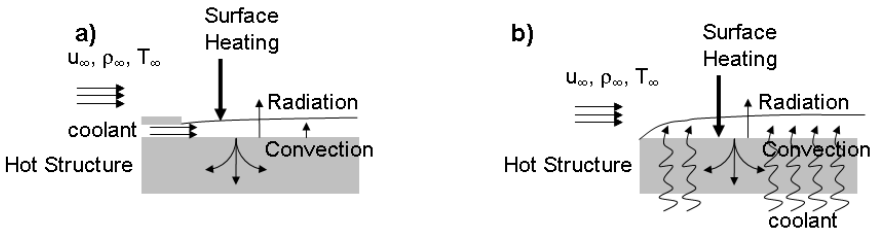

Figure 14: *a) Film-cooling and b) transpiration-cooling.*

by the active cooling. Two kinds of convective cooling, film and transpiration-cooling, are shown in Figure 14.

For film cooling, the coolant is injected into the external flow of atmospheric gas at a discrete upstream location. It blocks off the heat from the wall like a thin, insulating blanket. The surface heat balance, equation (7) turns into

$$\dot{q}_{F-S} = \dot{q}_{rad} + \dot{q}_{cond} \tag{13}$$

with index $F - S$ indicating convective heat transfer from the coolant film to the wall. Then, in order to determine the film temperature, another boundary condition is needed. Heat flux from the hot flow $\dot{q}_{HG-F}$, for example the surrounding atmospheric gas, heats up the film which in turn heats the wall over a length Δl. At the same time, cool flow with flow enthalpy h_{in} is flowing in from upstream and is heated up before it exits the film of film thickness δ_F on the downstream side with increased flow enthalpy h_{out}

$$\left(\dot{q}_{HG-F} - \dot{q}_{F-S}\right) \Delta l = \left((\rho u h)_{out} - (\rho u h)_{in}\right) \delta_F. \tag{14}$$

Turbulent flow is characterized by a strong vorticity, leading to a mix between the two gas flows, hot and film, reducing the cooling efficiency. In the heat balance of the coolant film as of eq. (14), the term of convection between hot gas flow and film can be replaced by a term $\dot{m} h_\infty$ accounting for the entraining hot gas mass into the film and the subsequent heat adjustment between the fluids [18]. Equation (14) becomes

$$\dot{m} h_\infty - \dot{q}_{F-S} \Delta l = -\left(h \rho u\right)_{in} \delta_{in} + \left((\rho u)_{in} \delta_{in} + \dot{m}\right) h_{out} \tag{15}$$

with growing film thickness δ_F. The factor $\dot{m}$ describes the mass of air entering into the film [22].

In transpiration-cooling, a coolant is fed through a porous and permeable wall structure to the outer mold line of a hot structure and there it forms a film. In contrast to the discrete locations used in film-cooling (a slit or hole), this is done over large areas. The structure is cooled by both convection, as the coolant passes through the pores, and by the film that has formed on the hot-gas side. A coolant film may also provide oxidation protection for the structure, which may be an important issue in case of carbon-based materials.

The heat balance on the hot side, according to eqs. (14) and (15), remains for both laminar or turbulent flow conditions. The cooling of the inner structure of the porous material is carried out by convective heat transfer between the material and the coolant. Radiation within the porous structure is negligible. According to Glass, the heat equation (4) for the wall material depending on coolant temperature T_C is extended to [23]

$$\rho c \frac{\partial T}{\partial t} = \lambda_x \frac{\partial^2 T}{\partial x^2} + \lambda_y \frac{\partial^2 T}{\partial y^2} - \alpha_V \left(T - T_C\right). \tag{16}$$

An additional balance for the coolant yields

$$-\frac{\partial\left(\frac{\dot{m}(x,y)}{A}c_{p,C}T_C\right)}{\partial x}-\frac{\partial\left(\frac{\dot{m}(x,y)}{A}c_{p,C}T_C\right)}{\partial y}+\alpha_V\left(T-T_C\right)=\rho_C c_{pC}\frac{\partial T_C}{\partial t}\,. \tag{17}$$

When only the pressure gradient in flow direction is taken into account, the above equation yields

$$-\frac{\dot{m}}{A}\frac{\partial\left(c_{p,C}T_C\right)}{\partial y}+\alpha_V\left(T-T_C\right)=\rho_C c_{pC}\frac{\partial T_C}{\partial t}, \tag{18}$$

with the volumetric heat transfer coefficient α_V, wall temperature T, coolant mass flow rate $\dot{m}$ and transpiration-cooled area A. The coolant density ρ_C is determined via the pressure distribution caused by a pressure difference between inside and outside. The pressure distribution within a porous material is commonly described by variations of Darcy's law

$$-\nabla p=\frac{\mu}{k_D}\vec{v}\,. \tag{19}$$

In this equation, ∇p is the pressure gradient in all directions, which is dependent on the flow velocity v in all directions, the viscosity $\mu(T_C)$ of the fluid and on the Darcy coefficient k_D.

The computer program HEATS (Heat Exchange Analysis for Transpiration Systems) serving to solve the heat balances of re-entry vehicle structures uses the set of equations given above [18]. HEATS determines transient wall temperature throughout an entire re-entry trajectory at short calculation time. It can thus be used as a lay-out tool for cooled or uncooled structures for both, in-flight and ground testing, so that overdesign can be minimized. This way, the thermal response of the structure is determined for the uncooled case as well as for coupled film- and convection cooled conditions. It has been validated by comparison to experiments in an arc-heated wind tunnel under laminar in-flow [18, 24]. HEATS will be referred to in a later section of this chapter when flight data is shown and evaluated.

3 MATERIAL CHOICE

As mentioned above, thermal protection systems (TPS) consist of structural parts, hot structural parts, attachment components and possibly a system infrastructure (such as gas or a liquid reservoir for active cooling). Flight vehicle substructures are commonly metal frames with good thermal conductivity, so that hot spots are avoided where hot parts are attached. The ideal candidate for the hot side of the TPS are ceramic materials, specifically carbon fiber composites, which are lightweight and have high specific strength and stiffness. They also have high emissivity at relatively low thermal conductivity which is necessary when insulated hot structures are used. The materials of the hot structures should typically have little to no erosion rate, e.g. due to oxidation or nitridation, and low surface catalycity, so that recombination of atomic species at the material surface is suppressed. Finally, they have to have compatible thermal expansion with their substructure, possess a high tolerance for cyclical loading and to be able to form complex shapes. Their purpose in hot structures is to handle the forces and temperatures experienced by leading edges in atmospheric re-entry and sustained hypersonic flight.

Carbon fiber composites have weak fiber-matrix bonding and higher matrix modulus than fiber modulus. This results in improved damage tolerance due to fiber pull-out, as shown in Figure 15. Since carbon fiber composites are lightweight and have stable properties even at high temperatures with respect to Young's modulus, strength, stiffness and tensile stretch, they are much applied for thermal protection of outer skins. The fibers increase damage tolerance and tensile strength of the ceramic while still being temperature and wear resistant. They also reduce the thermal expansion of the material. This is useful in structures that are subject to large thermal gradients, so thermal stress does not affect the component greatly. As opposed to monolithic ceramics, it is possible to manufacture ceramic parts that are even thin-walled, large or complexly shaped with the structural properties of these materials. Carbon fiber reinforced silicon carbide production techniques include liquid polymer infiltration [25], chemical vapor infiltration and liquid silicon infiltration.

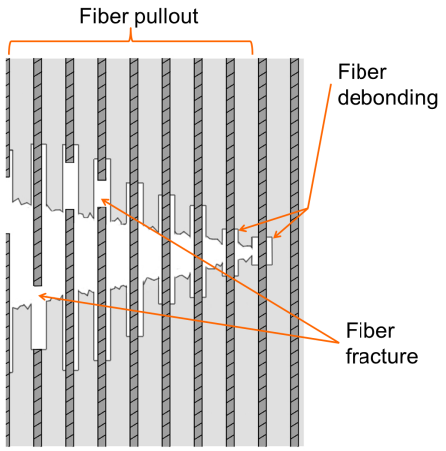

Figure 15: *Fiber pull-out.*

Besides being high temperature capable, material and more specifically the hot structure needs to be damage tolerant and provide stability versus combined loads over a large number of load cycles. The critical components include leading edges, control surfaces, acreage TPS, and seals. For the choice of the TPS high temperature material, ceramic matrix composites (CMCs) are becoming increasingly important for high temperature applications. New production methods for processing carbon fibers, innovative machines offering a wide range of lay-up possibilities as well as process development on infiltration methods or on metal-ceramic-joining enable increased use of these composites. In terms of space propulsion, for example, fiber reinforced nozzle extensions are being developed and tested, such as the Vinci nozzle by Snecma in France (Safran Group). Airbus Defence & Space has also been developing reinforced silicon carbide nozzle extensions for the ARIANE 5 first and upper stage motors as well as ceramic combustion chambers of smaller motors [25]. European missile company MBDA (France) and Airbus Defence & Space are moreover developing a fuel-cooled CMC combustion chamber for dual-mode ramjets (PTAH-SOCAR). It makes use of woven carbon fibre to produce the shape of the structure wanted with subsequent densification and, as fibrous structures are permeable, a sealant application process is used to seal the pre-form.

Another carbon fiber composite widely used is reinforced carbon-carbon (RCC), which was also used for

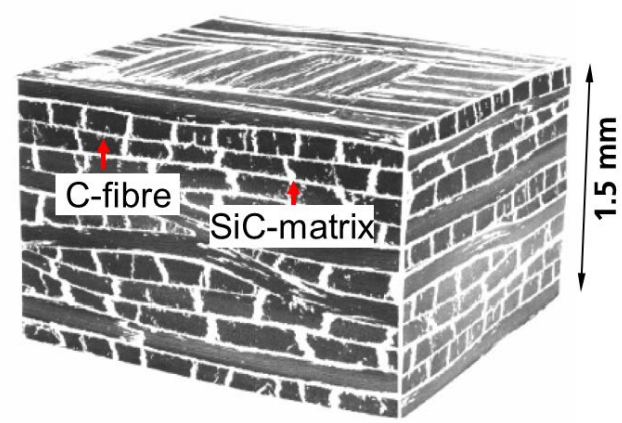

Figure 16: *Micro-structure of C/C-SiC [28].*

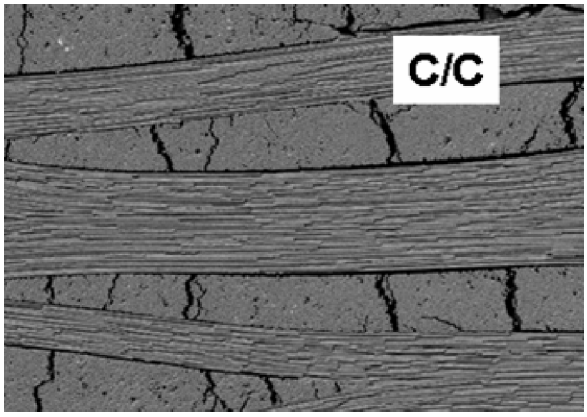

Figure 17: *Micro-structure of C/C with micro-cracks visible.*

the Space Shuttle Orbiter leading edges. It is manufactured by pyrolizing a nylon cloth, converting it to graphite. The graphite is then impregnated with a phenolic resin and cured in an autoclave. The cured material is pyrolized again to transform the cured resin to carbon. The part is then densified by impregnating it with furfural alcohol in a vacuum and pyrolizing a third time for carbon transformation. The densification step is repeated three times until the final RCC part has achieved a density of 1440 to 1600 kg/m^3 [26, 27]. An example of an RCC leading-edge is the X-43 Mach 10 vehicle leading edge, which was designed to reach nearly 2450 K during the short 130-second flight [21].

One example for a ceramic matrix composite, DLR's C/C-SiC, is shown in Fig. 16. The material is based on carbon fibers with a carbon and silicon carbide matrix. The fiber lay-up is typically a stack of 0/90° planar laminae so that the material is orthotropic and directional. Within the laminae planes and parallel to the fibers are the 0° and 90° direction, while the material can also be oriented at any other angle. It has a relatively low porosity of 3% and a low overall density of 1900 kg/m^3. The thermal expansion is low with of 2×10^{-6} K^{-1} parallel and 6×10^{-6} K^{-1} perpendicular to the fiber. The material has high specific strength at high temperatures up to 1840 K and is thermo-shock resistant. Since it is made with carbon fibers it has compromised oxidation resistance. C/C-SiC has been qualified in plasma wind tunnel testing and during real re-entry flight, such as in the FOTON 9, EXPRESS, FOTON-M2, and SHEFEX I and II missions [29–33]. The nose cap of the X 38 was developed, fully qualified and set up [34].

The fiber ceramic C/C-SiC is manufactured in house at DLR [28] with liquid silicon infiltration. The process is described here as an example for the manufacturing of CMC components. Firstly, a green body is made from carbon fiber reinforced plastic. Secondly, the green body is treated by pyrolysis under a pure nitrogen atmosphere at 1170 K and, thus, the matrix is carbonized to C/C. In the second step, a micro crack pattern is formed within the carbon matrix. This intermediate stage C/C has intriguing permeable properties. The good permeability of the C/C produced during DLR's pyrolysis step, is used in transpiration cooling in which a cooling fluid is fed trhough the structure into the boundary layer, as described in section 2. The micro-cracks in the low density carbon matrix serve as open pores for the fluid transfer. The pores distribute the coolant evenly over the hot facing surface to keep it cool and enable it to withstand exposure to high temperatures. The permeability of the C/C used for the hypersonic in-flight transpiration-cooling experiment AKTiV in 2012 is

Figure 18: *Sintered bronze as offered by Koldamex Stahl GmbH.*

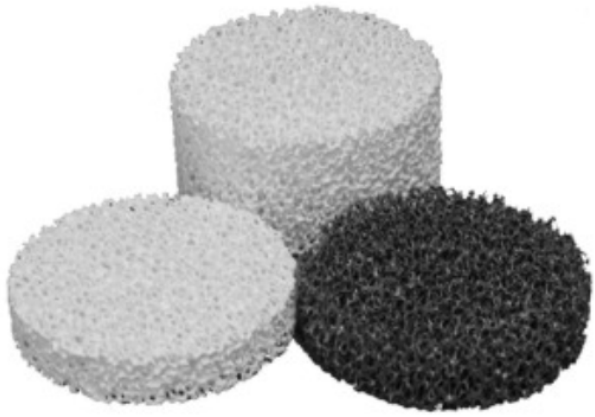

Figure 19: *Ceramic sponges as investigated at TVT Karlsruhe.*

on the order of $10^{-13}\,\mathrm{m}^2$. The porosity is relatively high at 12%. A coolant film may also provide oxidation protection for the structure.Since material properties are adjustable by choice of rovings and stacking of plies, both conductivity and permeability can be optimized to the values necessary for the application. The third step towards C/C-SiC contains the liquid infiltration of the C/C-body with silicon under vacuum at 1870 K. Silicon carbide is formed, starting at the phase interfaces between silicon and carbon, until the entire matrix is transformed to silicon carbide. Meanwhile the fibres remain unaffected and a content of free silicon of approximately 2% remains.

For transpiration- or effusion-cooling, permeable material, i.e. a sponge with open pores, like C/C, is necessary. Other material possibilities are sintered metals like bronze or stainless, as shown in Fig. 18. For increased temperatures, there are also ceramic sponges, for example of SiSiC, SiC, Al2O3 or mullite, as used for example in porous burners and depicted in Fig. 19. According to the application, it has to be determined what material meets the load case. A porous oxide-ceramic nozzle which is cooled by soaking the pores with water might need to be fiber reinforced when it is connected with a combustion chamber that transfers stron vibration from combustion instabilities. Or can the material be cooled efficiently enough for it to be made from metal? Finally, chemical compatibility of material and coolant or its evaporating educts should be guaranteed.

4 TRANSPIRATION COOLING

The previous chapters have shown that the outer surface of hypersonic vehicles is subjected to severe aerodynamic heating. Especially for sharp edges at the stagnation point, the loads are immense. However, stability of the outer mold line is important since it impacts performance. Sharp leading edges at an airbreathing propulsion system generate shocks which are necessary to maximize airflow into the engines. Therefore, leading edges should not ablate, even when they are expendable parts. Instead, they may have to be actively cooled.

Cooling methods, as indicated above, include backface cooling, for example with a heat pipe, and film cooling, where the variants differ according to the method of gas effusion. Gas can be exhausted via a slit, a porthole or an array of holes or a randomly porous interface. Eckert and Livingood have shown in the 1950s that transpiration-cooling is an effective method compared to the other methods [35]. At that time, however, it was only possible to manufacture porous metal sponges for surface cooling that melt at relatively low temperature and are, thus, not adequate for space applications. The studies focused mainly on aircraft propulsion, but were soon applied to investigation of blunt body cooling of re-entry vehicles as well.

Modern regeneratively cooled cryogenic combustion chambers rely on metallic designs and are highly optimized. Within a regeneratively cooled rocket engine, the fuel is usually routed around the outer surface of the inner liner and opposite the hot gas flow towards the injector faceplate before being injected. Thereby, sufficient heat can be exchanged to protect the predominant inner copper wall. However, in an environment of roughly 3500 K in the hot combustion zone and a few hundred Kelvin in the cooled exterior of the chamber wall, thermal fatigue problems occur due to the high thermal expansion of metals, thus, limiting the engine cycles.

Figure 20 shows a radial cut view through a transpiration-cooled combustion chamber. The primary structure, a reinforced plastic, provides the structural integrity of the chamber by absorbing the mechanical loads induced by the chamber pressure. At the same time, it is a diffusion barrier for the hydrogen. The porous ceramic inner liner is cooled by a fraction of the cryogenic fuel passing through the material [2, 37]. Cooling efficiency was proven by subscale testing. Both structural integrity as well as thermo-chemical resistance are given, providing operational safety and since CMCs encounter only little thermal expansion, the liner does not face fatigue. Another advantage might be the smaller pressure loss upon injection due to missing cooling channels.

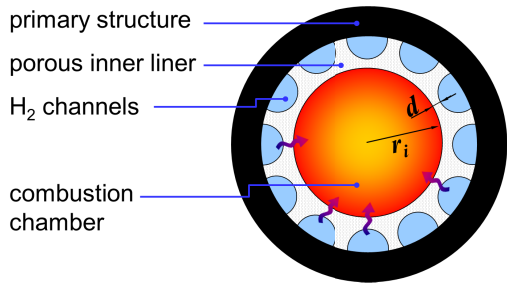

Figure 20: *Transpiration-cooling concept for combustion chamber application (cut-view).*

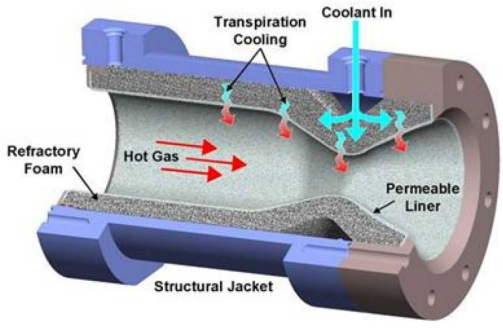

Figure 21: *Transpiration-cooling combustion chamber developed by AFRL [36].*

A similar concept is investigated at Ultramet (US), using three components: the outer jacket for structural support, an intermediate permeable core (a $MoSi_2$ or SiC-foam) and a porous inner liner, a mixed molybdenum disilicide-silicon carbide [36]. Moreover, the permeable structure can be used for porous injection. Capra et al. have fed fuel through an oxide based CMC in a scramjet engine tested in a shock tunnel at Ma around 9.5 and have detected thrust improvement as opposed to the more common porthole

injection [7, 38].

Concepts based on porous transpiration or effusion-cooled CMC structures have been and are currently investigated within the programs IMENS [39], ATLLAS, and the DFG Research Center TRR40 [40]. A variety of mass flow rates and porous materials are under investigation. Also, different coolant media, such as helium, nitrogen, air and argon, are tested. Wolf states that the amount of a gas-coolant required to provide a certain amount of transpiration-cooling of a body is approximately inversely proportional to the heat (or cooling) capacity of the gas according to $\dot{m} \sim \frac{1}{c_p}$ [41]. In further investigations, liquids are used as a coolant [42]. They have the advantage that the heat of vaporization can be used as an additional cooling mechanism. Water is a candidate frequently studied because it has a high heat of vaporization of 4168 J/kg K and is cheap and available. However, care must be taken so that carbon fibers do not oxidize in the water vapour.

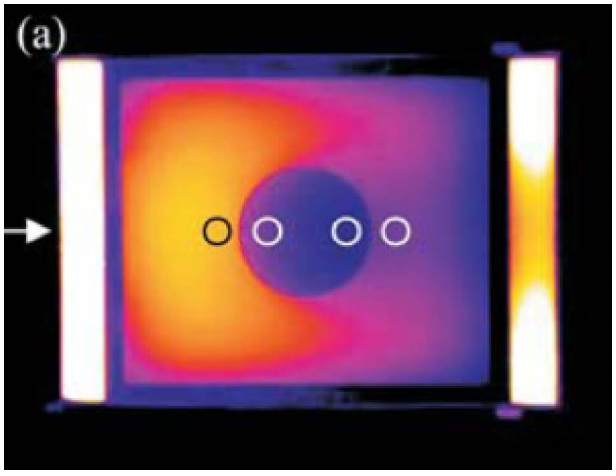

Figure 22: *IR-thermography of a circular transpiration-cooled C/C sample in an arc-jet [39].*

This technology, in which a coolant is forced through a permeable wall component by a pressure gradient, has recently been used for re-entry load cases. There is yet to be a fully integrated actively cooled TPS design, withstanding both thermal and mechanical loads. However, AKTiV (Aktive Kühlung durch Transpiration im Versuch), the first hypersonic flight experiment of a transpiration-cooled TPS element, was flown in the suborbital atmospheric re-entry body SHEFEX II in 2012 [3].

The transpiration-cooled experiment AKTiV was a key experiment of SHEFEX II, monitoring an actively transpiration-cooled thermal protection panel during hypersonic return flight [43]. In order to interpret the cooling effect of the transpiration, AKTiV was fitted with thermocouples, as well as pressure sensors and resistance thermometers. The experiment, using a porous and permeable C/C ceramic, was located onto a dedicated panel (C3, as shown in Fig. 10). A non-pressurized reference set-up was mounted on the opposite panel (C7) where the same ambient flow conditions were expected. Although this location was not subject to extreme heat load for the SHEFEX II trajectory, the findings serve to support theories for future structural design with transpiration-cooling.

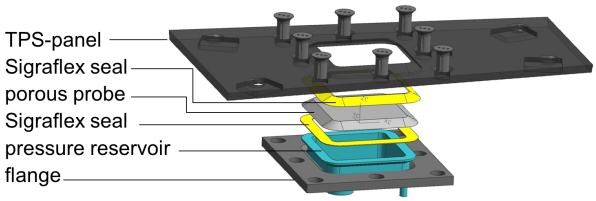

Figure 23: *AKTiV experiment set-up.*

Figure 24: *AKTiV side view.*

Figure 23 shows the AKTiV experiment set-up. A porous C/C 5 mm-thick sample of the dimensions $61 \times 61\,\mathrm{mm}^2$ was inserted in the center of a 7 mm-thick thermal protection panel. The coolant, here nitrogen,

was run through the porous sample, which was flanged into the surrounding TPS-panel by a pressure reservoir and riveted ceramic fasteners [44, 45]. The reservoir itself is made of stainless steel. The panel and sample are sealed against sneak flows by graphite Sigraflex felt.

The system consists of a pressurized tank, a pressure regulator, a valve on the vehicle side of the experiment and another pressure regulator, a mass flow controller (sonic nozzle), sensors and data acquisition hardware on the payload side of the experiment. A photograph of the entire set-up is shown in Fig. 24. Thermocouples shall serve to monitor the effect of the film-cooling redundantly, specifically downstream of the porous sample, but also locally resolved, as designated by the white numbers in Fig. 25. The reference module on panel C7, monitoring the uncooled behaviour of the set-up, is indicated by black numbers in Fig. 25.

Figure 25: *AKTiV thermocouple locations.*

Cooling was switched on via telecommand at 431 s into the SHEFEX II flight. It can be seen in Fig. 26 that when the coolant began to flow, the temperatures of the panel decreased, showing the effect of the transpiration-cooling. This is demonstrated by measurement on the porous sample itself, but also in the film-cooling region downstream of the sample. The temperature difference with respect to the uncooled reference setup was largest at location K38 with 87 K, which corresponds to a cooling efficiency of 58%. Downstream of the sample, the temperature was effectively reduced by 74.5 K at K33, resulting in a cooling efficiency of 42% [43]. A cooling effect on the order of 11% can even be noticed upstream of the sample, and it is assumed that heat conduction causes this cooling effect.

The transverse temperature distribution in the downstream region of the cooled sample is shown in Fig. 27. The lowest temperature, i.e. the highest temperature reduction, was measured at the centermost thermocouple while the outermost thermocouples registered the highest temperatures. This corresponds well to the expected coolant film behaviour, where flow from the vicinity is entrained into the coolant film. Figures 28 and 29 show that the cooling is reproduced by the computer program HEATS, described in section 2, with only small deviations on the porous sample. Figures 26–29 also show the interesting effect that the temperatures increase again after being cooled down from the time at whihc the coolant was turned on. This shows that the structure is not overcooled and still reacts to increasing heat flux. This is supported by the simulations in HEATS [43].

The measurements of AKTiV at t=485.12 s are plotted over disctance x from the panel edge in Fig. 30. The starting temperature chosen for the simulation with HEATS was the average of the panel temperatures at 431 s.

The result for the uncooled panel C7 shows good agreement with the measurement for the data from C/C-SiC, i.e. the panel into which the sample is embedded. Far higher deviations are observed at the C/C-sample of AKTiV (0.7445 m – 0.8055 m), which are attributed to the heat sink effect of the stainless reservoir. In the HEATS calculation, the temperatures of the C/C are higher than those of the C/C-SiC because of both lower thermal conductivity and a thinner sample thickness. However, in the flight measurement, the temperatures are reduced by the set-up with the reservoir.

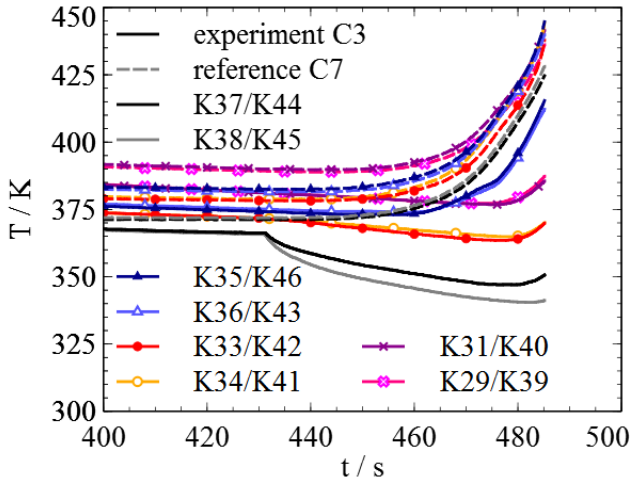

Figure 26: *Temperatures on AKTiV and the reference setup upon re-entry [3].*

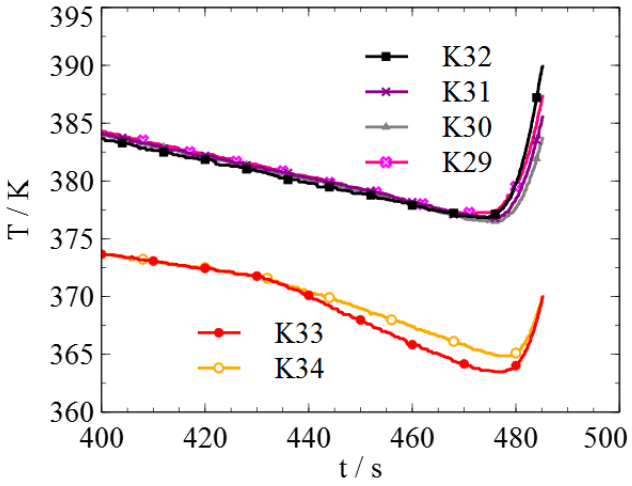

Figure 27: *Measured temperature transverse to the panel in first and second downstream location. [3]*

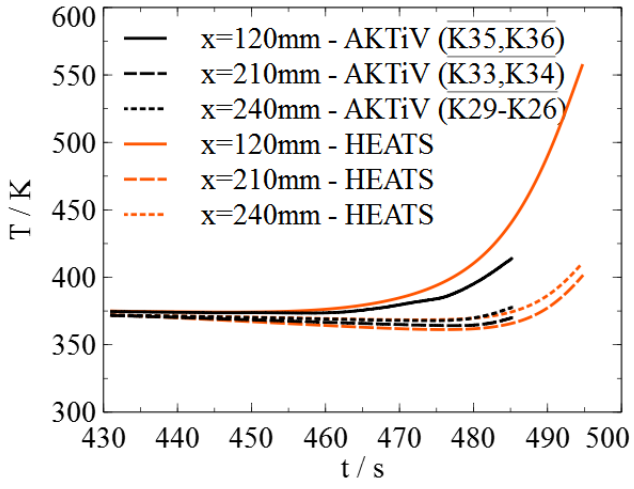

Figure 28: *Comparison of HEATS with up- and downstream measurement.*

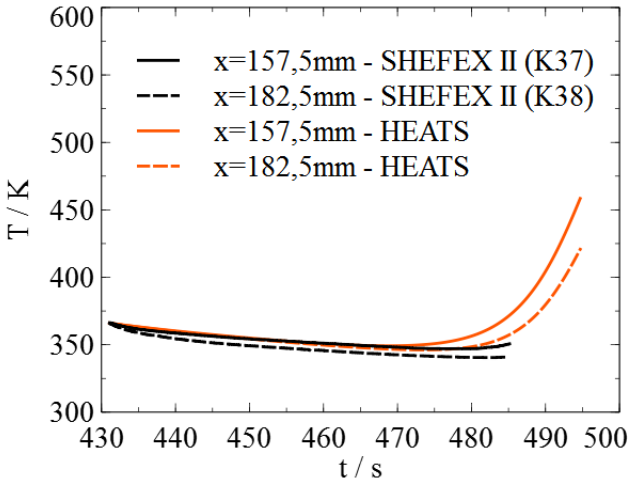

Figure 29: *Comparison of HEATS with data from the cooled sample.*

Being able to reproduce the AKTiV results and those of ground testing experiments, e.g. a shock tunnel campaign [24] or the IMENS data from the arc-heated wind tunnel [18], mentioned above, helps to identify other parameters that have not been measured. For example, heat flux to the structure can be reproduced although not measured or temperatures at locations that have not been equipped with thermocouples. Moreover, the simulation with HEATS can be used for future TPS lay-out. The parameter study shown in Figs. 31 and 32 can be used by the designer as a look-up table to identify how much mass flow rate is needed to reduce the temperature to a certain level supported by the material. Fig. 31 gives net heat flux for each flow condtion which is referred to as a hot wall heat flux. The flow conditions are defined in terms of p, v and T of a flow and are given in the table. They are chosen along a potential flight trajectory and thus differ mostly in pressure. Fig. 32 gives surface temperature for the respective flow conditions that would result in the labeled hot wall heat flux if it remained uncooled.

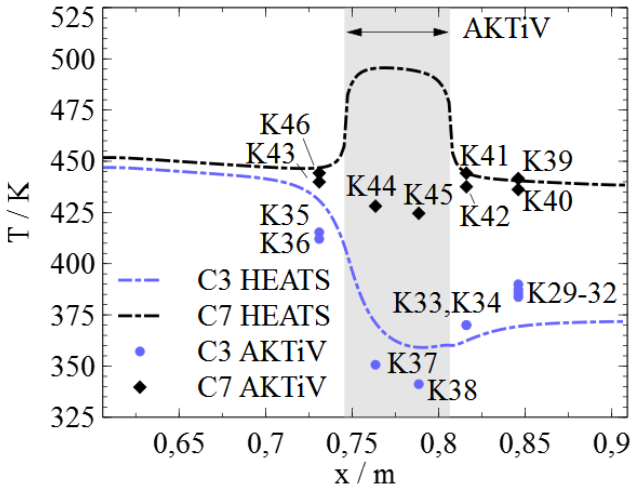

Figure 30: *AKTiV temperatures along panel C at t=485.12 [3].*

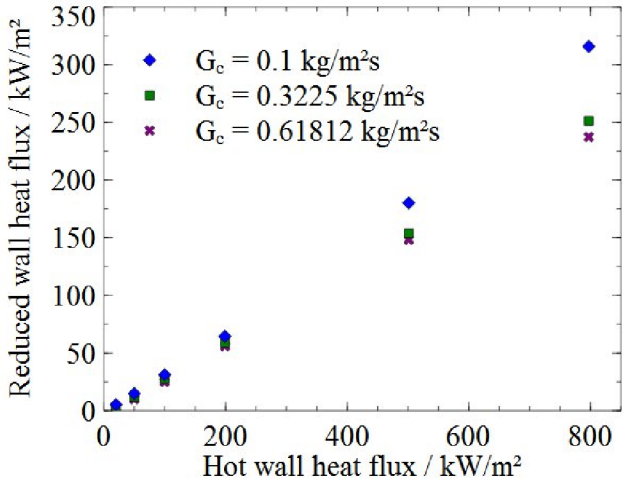

Figure 31: *Wall heat flux reduction according to uncooled heat flux and G_c=$\dot{m}/A$.*

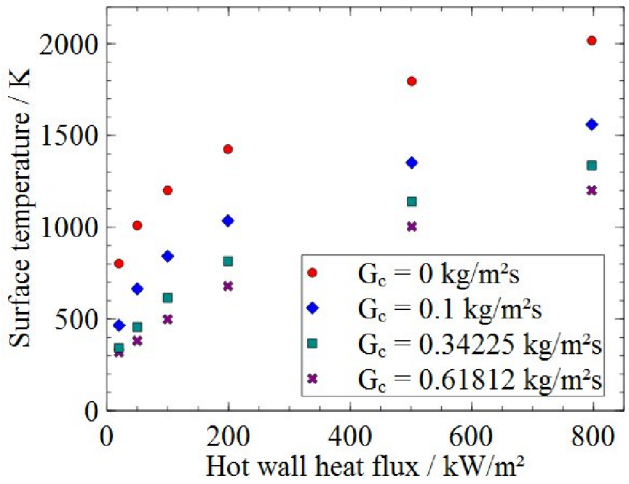

Figure 32: *Surface temperature reduction according to mass flow rate and flow condition.*

q_{uc}	20	50	100	200	500	800
p	29,73	192,36	792,64	3247,13	23105,96	69764,78
T	1144	1191	1231	1212	1170	1120
v	4857	4880	4898	4911	4881	4766

5 PERSPECTIVE

The presented study shows the potential of advanced composite materials for the development of hypersonic flight through transpiration-cooling. However, sharp leading edges promote stagnation areas causing strong temperature gradients, and thus stress in the permeable material. Moreover, since the heat load is most severe in the tip of the leading edge, it will become necessary to direct more coolant there than anywhere downstream of the tip. This is also important because the stagnation area is not film-cooled by coolant from an upstream region. Because this is the case downstream, less coolant transpiration is needed, there. On the other hand, for a phase in which an angle of attack is flown, the coolant must be directed towards the chin panel. Transpiration-cooling must be thoroughly investigated to see if it can serve efficiently in a TPS for orbital or higher atmospheric velocities.

Prediction tools for three-dimensional transpiration-cooling are needed in order to design, for example, the SHEFEX III leading edge. This includes the transient computational simulation of the cooled leading edge's thermal response. The simulation must be capable of considering strong gradients of all state variables. Moreover, it must compute the coolant distribution in the cooled wall at thermal non-equilibrium between coolant and structure and at wall pressure gradients. Also, special emphasis is to be placed on investigation and exact simulation of the film-cooling region. Figure 33 shows its current design, with porous material at the chime

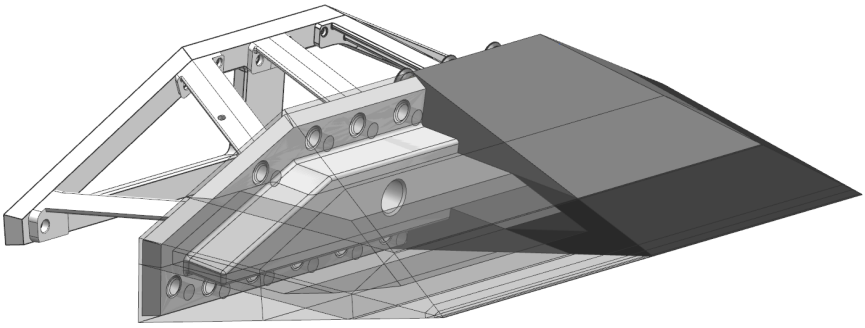

Figure 33: *Design of the SHEFEX III leading edge.*

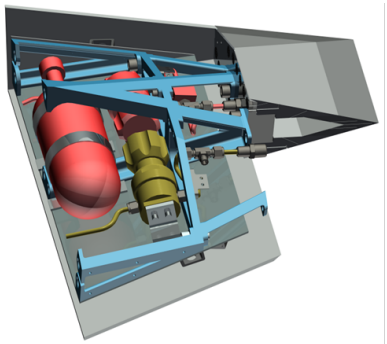

Figure 34: *SHEFEX III leading edge infrastructure.*

and film-cooled top and chin panels. Challenges include the prediction of necessary coolant mass flow distribution over the profile, including cooling efficieny in turbulent flow, realization of a graded permeability and directed mass flow rate in anisotropic porous material, attachment of the structure to the vehicle, tightening of the reservoir towards the porous structure and many other aspects.

Liu et al. have investigated a transpiration-cooled wedge geometry made from stainless steel with a nose radius of 8.72 mm and a porosity of 42.8% [46]. They used various gaseous media (air, N_2, He Ar, CO_2) for the cooling. They showed that the temperature gradients along the wall surface and cooling efficiency differ from those along a curved wedge geometry. The performance of water transpiration-cooling of a leading edge with phase change was investigated by Wang et al. [42]. The porous leading edge with 2 mm radius was made of sintered 316L alloy and is depicted in Fig. 35. The absolute porosity was 34%. They showed that a configuration with the thinnest wall thickness at the stagnation point provides enhancement of the cooling there.

In order to thoroughly study the flow phenomena in the porous structure, a transpiration-cooled C/C cone shown in Fig. 36 was investigated with focus on the varying cooling mass flow along the surface, caused by the anisotropic permeability of the material. Outflow behavior was measured by the dynamic pressure distribution

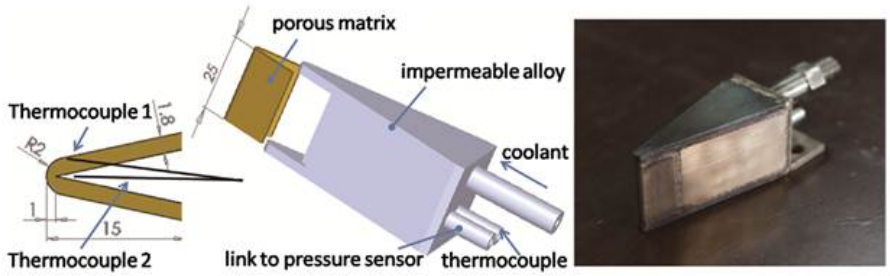

Figure 35: *Wind tunnel experiment setup for water transpiration-cooling [42].*

perpendicular to the outflow at the surface. For the measurements, a constant mass flow rate through the sample was established and a pitot sensor was stepwise moved along the flank of the cone [47]. It is important to note that the measurement angle of the pitot tube with regards to the fiber orientation and surface matters. Additionally, reservoir pressure and the total mass flow rate are surveyed.

Figure 37 shows the pitot measurement projected on cartesian coordinates when looking head-on to the tip of the cone. The x- and y-directions in the graph depict the line along the flank of the cone from tip to base. Colors represent the absolute measured pressure value and the measurement point diameter matches the pitot diameter. It is obvious from this representation, that with C/C from stacked 0°/90° plies a single measurement point is not representative and the material is strongly anisotropic. In contrast to the idealized, homogenous approach for a Darcy-flow as used in Eq. 19, discrete, small channels determine the outflow characteristic. However, the representation of 37 highlights, that the outflow is concentrated around two angles at approximately 160° and 340°, representing the flow direction parallel to the plies of C/C (see Fig. 36). On a macroscopic scale, this shows that the material has somewhat orthotropic properties, since the permeability underlies the fabric directions. The permeability k_D parallel to the plies is much higher than that of the perpendicular direction and thus most of the flow concentrates at the regions parallel to the plies. As expected, the cone has practically no flow at the tip region since the coolant has to penetrate higher wall thickness [47].

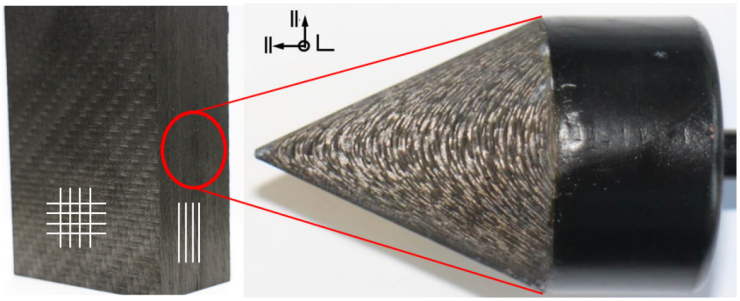

Figure 36: *C/C cone with indicated fiber orientation [47].*

The 2D-simulation of Fig. 38 of the pressure distribution with HEATS, introduced above, supports the measurement in terms of showing a large pressure distribution difference between perpendicular and parallel directions. The 2D calculation does not take into account potential circumferential flow within the cone that might originate from coolant escaping from the blocked perpendicular stack towards the free parallel stack. The boundary conditions were the reservoir pressure in the plenum and the ambient pressure outside the cone. However, since the measurement unveils strong jets overlaying low and inhomogeneous outflow pressure, the comparison of the measurement to the numerical results is difficult.

Should additional heat flux be applied, the coolant mass distribution in the structure plays a major role. As mentioned above, sharp leading edges offer only little volume and thus mass for heat capacity, the maximum heat flux impinges at the tip while the tip, in terms of design, mostly has the highest wall thickness for the coolant to pass. Additionally, upon high wall temperatures, heating up the coolant, the coolant expands.

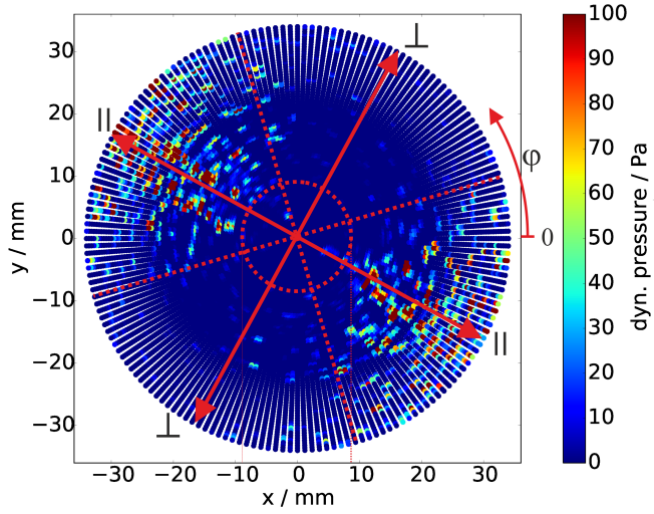

Figure 37: *Dynamic exhaust pressure contours [47].*

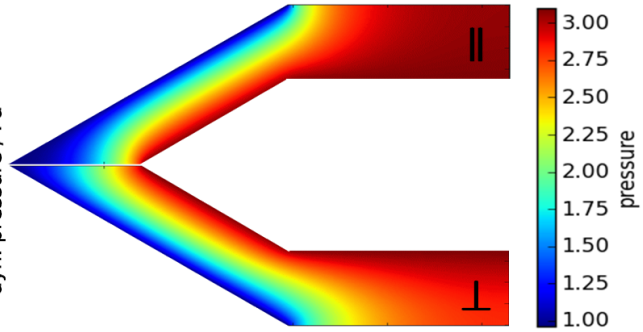

Figure 38: *Simulated pressure distribution in coolant with fiber orientation perpendicular and parallel to the radius [47].*

Coolant density decreases while, according to Sutherland, a gaseous coolant's viscosity increases. According to Eq. (19), both effects block the mass flow so that either mass flux is decreased or a higher feeding pressure is requested to supply the same mass flow rate.

The transpiration-cooled wedge-shaped CMC leading edge simulation in a modified numerical solver based on the OpenFOAM environment demonstrates the anisotropy influence of the material under heat load [48]. As above, different coolant mass flow distributions are determined depending on the fiber orientation of the considered ceramic wedge. The contour plot of Fig. 39 represents the material temperature of the porous wedge. Darcy streamlines illustrate the two-dimensional coolant gas flow path in the structure and vector arrows depict the fluid velocity at the in- and outflow boundary. It is observed that the solid temperatures decrease to relatively low values with distance from the wedge tip. This is due to both, lower incoming heat flux compared to the tip region and an improved cooling situation because of smaller wall thickness.

The temperature for case A is generally higher in comparison to case B. This is especially pronounced for the front part of the sharp structure. Due to a much lower permeability along the direction of the symmetry line for case A, less coolant gas is transported to the front region. As can be seen from the Darcy streamlines, the flow path is curved and the coolant exits the structure aligned with the direction of highest permeability, i.e. parallel to the plies. In case B, more coolant mass flow is directed to the front region instead of taking the shorter path through the wedge's side wall. In accordance to this, it can also be noted that the coolant velocity is slightly turned towards fiber direction in the aft region.

A fiber orientation parallel to the geometry's symmetry line is found to be favorable in terms of cooling of the hot wedge tip. In contrast, the necessary pressure difference in order to induce a specified coolant mass flow is higher compared to a wedge with perpendicular fiber orientation.

Although the general understanding of transpiration-cooling and that of anisotropic material is developing, the combination of the two is a challenge. There is for example the question of the effective exhaust velocity of the coolant from the porous medium which has unknown coolant passage geometry. Another point of interest

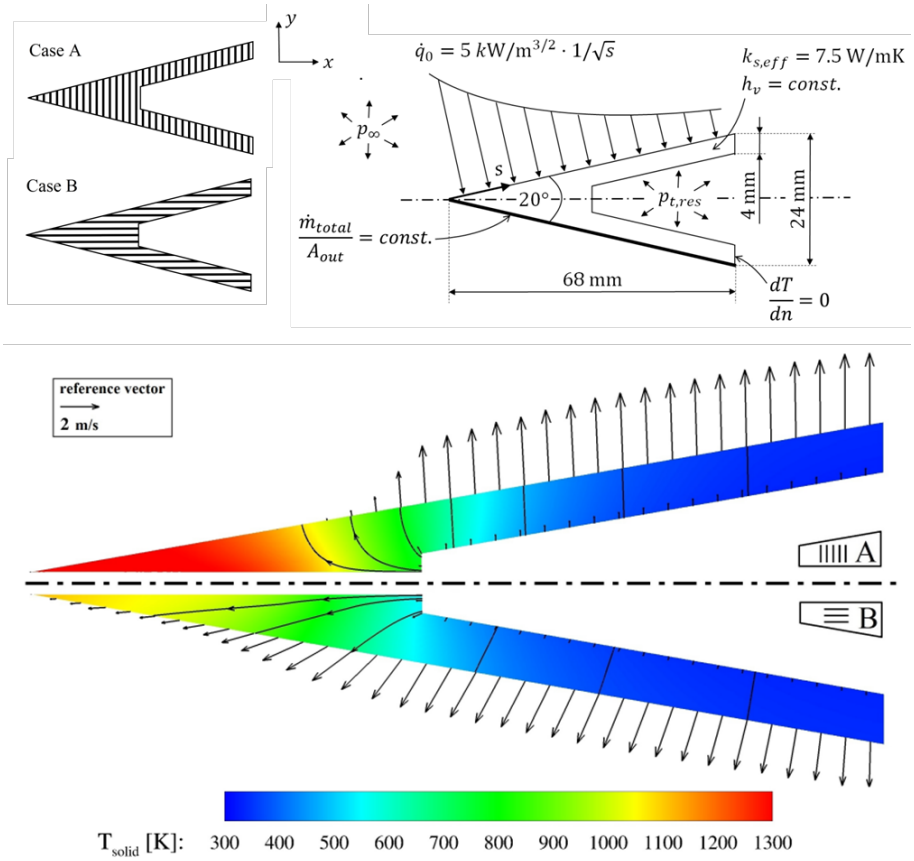

Figure 39: *Contour plot of solid temperature with Darcy streamtraces and fluid velocity vectors for fiber orientation perpendicular (A) and parallel (B) with respect to symmetry line [48].*

might be the transitioning of the boundary layer to turbulent flow caused by gas injection. Moreover, measurement of the volumetric heat transfer coefficient is tricky. How big does a structure have to be in order for the gereralized laws of heat transfer and permeation to be valid? How can I attach a porous element to a vehicle structure and how do I design parts in order for the flow to permeate them at exactly the points of interest? ...

Hannah Böhrk

REFERENCES

[1] Hald, H., Ortelt, M., Fischer, I., Greuel, D., and Haidn, O., "Effusion Cooled CMC Rocket Combustion Chamber," *13th AIAA/CIRA International Space Planes and Hypersonic Systems and Technologies Conference*, Capua, Italy, 2005, AIAA 2005-3229.

[2] Ortelt, M., Hald, H., Herbertz, A., and Müller, I., "Advanced Design Concepts for Ceramic Thrust Chamber Components of Rocket Engines," *Proceedings of the 5th European Conference For Aerospace Sciences (EUCASS)*, Munich, Germany, Jul. 2013.

[3] Böhrk, H., "Transpiration Cooling at Hypersonic Flight – AKTiV on SHEFEX II," *11th AIAA/ASME Joint Thermophysics and Heat Transfer Conference*, Atlanta, GA, 2014, AIAA 2014-2676.

[4] Böhrk, H., "Heat Flux Reduction by Transpiration-Cooling of CMCs for Space Applications," *Advanced Materials: Properties and Applications*, edited by E. Bafekrpour, DeGruyter, 2015, in print.

[5] Oertel Jr., H., *Aerothermodynamik*, Springer-Verlag, Berlin Heidelberg, 1994.

[6] Hirschel, E. and Zarchan, P., *Basics of Aerothermodynamics*, No. 206 in Progress in Astronautics and Aeronautics, Springer, 2006.

[7] Capra, B., Boyce, R., Kuhn, M., and Hald, H., "Porous Versus Porthole Fuel Injection in a Radical Farming Scrmjet: Numerical Analysis," *Journal of Propulsion and Power*, Vol. 31, No. 3, 2015, pp. 789–804, doi: 10.2514/1.B35404.

[8] Marvin, J. and Pope, R., "Laminar Convective Heating and Ablation in the Mars Atmosphere," *AIAA Journal*, Vol. 5, No. 2, 1968, pp. 240–248.

[9] Longo, J., Eggers, T., Gülhan, A., Turner, J., and Weihs, H., "Designing Flight Experiments for Hypersonic Flow Physics," *Lecture Series "Flight Experiments for Hypersonic Vehicle Development"*, RTO AVT VKI Lecture Series, Brussels, Belgium, 2005.

[10] Strohmeyer, D., Eggers, T., and Haupt, M., "Waverider Aerodynamics and Preliminary Design for Two-Stage-to-Orbit Missions, Part 1," *Journal of Spacecraft and Rockets*, Vol. 35, No. 4, 1998, pp. 450–458.

[11] Eggers, T., Novelli, P., and Haupt, M., "Design Studies of the JAPHAR Experimental Vehicle for Dual Mode Ramjet Demonstration," *10th AIAA/NAL/NASDA/ISAS International Space Planes and Hypersonic Systems and Technologies Conference*, Kyoto, Japan, 2001, AIAA 2001-1921.

[12] Reuther, J., Kinney, D., Smith, S., Kontinos, D., Gage, P., and Saunders, D., "A reusable space vehicle design study exploring sharp leading edges," *35th AIAA Thermophysics Conference*, Anaheim, CA, 2001, AIAA 2001-2884.

[13] Arnold, J., Johnson, S., and Wercinski, P., "SHARP: NASA's Research and Development Activities in Ultra-High Temperature Ceramic Nose Caps and Leading Edges for Future Space Transportation Vehicles," *52nd International Astronautical Congress*, Toulouse, France, 2001, IAF paper 01-V.5.02.

[14] Weihs, H., Turner, J., and Longo, J., "The Sharp Edge Flight Experiment SHEFEX II, a Mission Overview and Status," *15th AIAA/DLR/DGLR International Space Planes and Hypersonic Systems and Technologies Conference*, Dayton, USA, 2008.

[15] Weihs, H., Longo, J., and Gülhan, A., "The Sharp Edge Flight Experminet SHEFEX," *4th European Workshop on Thermal Protection Systems & Hot Structures Conference Proceedings*, European Space Agency, Noordwijk, The Netherlands, 2002, SP-521.

[16] Turner, J., Ettl, J., Hörschgen-Eggers, M., Turner, P., and Jung, W., "SHEFEX II Vehicle and Subsystem Design, Flight Performance and their Application to Future Hypersonic Missions," *Proceedings of the 21st ESA Symposium on European Rocket and Balloon Programmes and Related Research*, No. ESA SP-721, European Space Agency, Noordwijk, the Netherlands, 2013, pp. 137–142.

[17] Böhrk, H., Elsäßer, H., and Weihs, H., "The SHEFEX II Thermal Protection System," *7th Symposium on Aerothermodynamics for Space Vehicles*, European Space Agency, Brugge, Belgium, 2011, ISBN 978-92-9221-256-8. ISSN 1609-042X.

[18] Böhrk, H., Piol, O., and Kuhn, M., "Heat Balance of a Transpiration-Cooled Heat Shield," *Journal of Thermophysics and Heat Transfer*, Vol. 24, No. 3, 2010, pp. 581–588.

[19] van Driest, E., "Investigation of Laminar Boundary Layer in Compressible Fluids using the Crocco Method," *Tech. Rep. NACA TN-2597*, 1952.

[20] van Driest, E., "The Problem of Aerodynamic Heating," *Aeronautical Engineering Review*, Vol. 15, No. 10, 1956, pp. 26–41.

[21] Glass, D., "Ceramix Matrix Composite (CMC) Thermal Protection Systems (TPS) and Hot Structures for Hypersonic Vehicles," *15th AIAA/DLR/DGLR International Space Planes and Hypersonic Systems and Technologies Conference*, Dayton, USA, 2008, AIAA-2008-2682.

[22] Goldstein, R., "Film Cooling," *Advances in Heat Transfer*, edited by T. Irvin and J. Hartnett, Academic Press, New York, 1971, pp. 321–379.

[23] Glass, D., Dilley, A., and Kelly, H., "Numerical Analysis of Convection and Transpiration Cooling," *Journal of Spacecraft and Rockets*, Vol. 38, 2001, pp. 15–20.

[24] Böhrk, H., Martinez Schramm, J., Wartemann, V., Eggers, T., and Hannemann, K., "Shock Tube Testing of the Transpiration-Cooled Heat Shield Experiment AKTiV," *18th AIAA/3AF International Space Planes and Hypersonic Systems and Technologies Conference*, Tours, France, Sep. 2012, in preparation.

[25] Schmidt, S., Beyer, S., Knabe, H., Immich, H., Meistring, R., and Gessler, A., "Advances Ceramic Matrix Composite Materials for Current and Future Propulsion Technology Applications," *Acta Astronautica*, Vol. 55, 2004, pp. 409–420.

[26] Kasen, S., *Thermal Management at Hypersonic Leading Edges*, Ph.d.-thesis, University of Virginia, 2013.

[27] Curry, D., Cunningham, J., and Frahm, J., "Space Shuttle Orbiter Leading Edge Thermal Performance," *Entry Vehicle Heating and Thermal Protection Systems: Space Shuttle, Solar Startprobe, Jupiter Galileo Probe*, edited by P. Bauer and H. Collicott, Vol. 85, AIAA, 1983.

[28] Heidenreich, B., Hofmann, S., Jemmali, R., Frieß, and Koch, D., "C/C-SiC Materials Based on Melt Infiltration - Manufacturing Methods and Experiences from Serial Production," *High Temperature Ceramic Matrix Composites 8*, edited by L. Zhang and D. Jiang, The American Ceramic Society, John Wiley and Sons, Hoboken, NJ, 2014, pp. 296 – 310.

[29] Hald, H., "CMC Materials: from Plasma Channel Testing to Real Capsule Re-Entry," *High Temperature Chemical Processes*, Vol. 3, April 1994, pp. 153–165.

[30] Hald, H., *Faserkeramiken für heiße Strukturen von Wiedereintrittsfahrzeugen - Simulation, Test und Vergleich mit experimentellen Flugdaten*, Dissertation, Universität Stuttgart, Fak. Luft- und Raumfahrttechnik, 2001.

[31] Reimer, T., "The KERAMIK Thermal Protection System Experiment on the FOTON-M2 Mission," *5th European Workshop on Thermal Protection Systems & Hot Structures Conference Proceedings*, European Space Agency, Noordwijk, The Netherlands, 2006, SP-631.

[32] Eggers, T., Longo, J., Turner, J., Jung, W., Hörschgen, M., Stamminger, A., Gülhan, A., Siebe, F., Requardt, G., Laux, T., Reimer, T., and Weihs, H., "The SHEFEX Flight Experiment – Pathfinder Experiment A for a Sky Based Test Facility," *14th AIAA Spaceplane Systems and Technologies Conference*, Canberra, Australia, Nov. 2006.

[33] Gülhan, A., Siebe, F., Weihs, H., Laux, T., Longo, J., Eggers, T., Turner, J., and Hörschgen, M., "The Sharp Edge Flight Experiment – a Mission Overview," *5th European Workshop on Thermal Protection Systems & Hot Structures Conference Proceedings*, European Space Agency, Noordwijk, The Netherlands, May 2006, SP-631.

[34] Weihs, H., Hald, H., Reimer, and T., Fischer, I., "Development of a CMC Nose Cap for X-38," *52nd International Astronautical Congress*, Toulouse, France, Oct. 2001.

[35] Eckert, E. and Livingood, J., "Comparison of Effectiveness of Convection-, Transpiration-, and Film-Cooling Methods with Air as Coolant," Tech. rep., NACA, 1954.

[36] Sözen, M. and Davis, P., "Transpiration Cooling of a Liquid Rocket Thrust Chamber Wall," *44th AIAA/ASME/ASEE Joint Propulsion Conference and Exhibit*, Hartford, CT, 2008.

[37] Greuel, D., *Untersuchungen zum Impuls- und Stofftransport in effusiv gekühlten faserkeramischen Raketenbrennkammerwänden*, Ph.d.-thesis, RWTH Aachen, 2013.

[38] Capra, B., Boyce, R., Kuhn, M., and Hald, H., "Combustion Enhancement in a Scramjet Engine using Oxygen Enrichment and Porous Fuel Injection," *Journal of Fluid Mechanics*, Vol. 767, 2015, pp. 173–198, doi: 10.1017/jfm.2015.43.

[39] Kuhn, M. and Hald, H., "Application of Transpiration Cooling for Hot Structures," *RESPACE - Key Technologies for Reusable Space Systems*, edited by A. Gülhan, Vol. 98 of *Notes on Numerical Fluid Mechanics and Multi- disciplinary Design*, Wiley-VCH, 2008, pp. 82–103.

[40] Langener, T., von Wolfersdorf, J., Selzer, M., and Hald, H., "Experimental Investigations of Transpiration Cooling Applied to C/C Material," *International Journal of Thermal Sciences*, Vol. 54, 2012, pp. 70–81.

[41] Wolf Jr., L., Obremski, H., and Christian, W., "Transpiration Cooling in an Arc-Jet Environment," *AIAA Journal*, Vol. 4, No. 4, 1966, pp. 747–749.

[42] Wang, J., Zhao, L., Wang, X., Ma, J., and Lin, J., "An Experimental Investigation on Transpiration Cooling of Wedge Shaped Nose Cone with Liquid Coolant," *International Journal of Heat and Mass Transfer*, Vol. 75, 2014, pp. 442–449.

[43] Böhrk, H., "Transpiration-Cooled Hypersonic Flight Experiment: Set-Up, Flight-Measurement and Reconstruction," *Journal of Spacecraft and Rockets*, Vol. 52, No. 3, 2015, pp. 674–683, doi: 10.2514/1.A33144.

[44] Ortelt, M., Rühle, F., Hald, H., and Weihs, H., "Dynamic qualification of a new CMC fastener," *High Temperature Ceramic Matrix Composites*, edited by W. Krenkel, N. R., and H. Schneider, ECI Symposium Series, Wiley-VCH Verlag GmbH & Co. KGaA, Weinheim, 2001, pp. 760–766.

[45] Böhrk, H. and Beyermann, U., "Secure tightening of a CMC fastener for the heat shield of re-entry vehicles," *Composite Structures*, Vol. 92, No. 1, Jan. 2010, pp. 107–112.

[46] Liu, Y.-Q., Jiang, P.-X., Jin, S.-S., and Sun, J.-G., "Transpiration Cooling of a Nose Cone by Various Foreign Gases," *International Journal of Heat and Mass Transfer*, Vol. 53, 2010, pp. 5364–5372.

[47] Dittert, C., Selzer, M., and Böhrk, H., "Characterization of the Flow Field of Anisotropic Porous Cones with Different Wall Thickness," *20th AIAA International Space Planes, Hypersonic Systems and Technologies Conference*, Glasgow, UK, Jul. 2015, AIAA 2015–3661.

[48] Prokein, D., von Wolfersdorf, J., and Böhrk, H., "Analysis of Anisotropy Effects for Transpiration Cooled CMC Leading Edges using OpenFOAM," *20th AIAA International Space Planes, Hypersonic Systems and Technologies Conference*, Glasgow, UK, Jul. 2015, AAA 2015–3552.